

Multidimensional dynamic piezoresponse measurements: Unraveling local relaxation behavior in relaxor-ferroelectrics via big data

Rama K. Vasudevan, Shujun Zhang, M. Baris Okatan, Stephen Jesse, Sergei V. Kalinin, and Nazanin Bassiri-Gharb

Citation: *Journal of Applied Physics* **118**, 072003 (2015); doi: 10.1063/1.4927803

View online: <http://dx.doi.org/10.1063/1.4927803>

View Table of Contents: <http://scitation.aip.org/content/aip/journal/jap/118/7?ver=pdfcov>

Published by the [AIP Publishing](#)

Articles you may be interested in

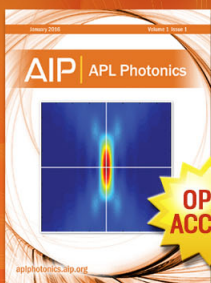
Piezoresponse force microscopy studies on the domain structures and local switching behavior of $\text{Pb}(\text{In}_{1/2}\text{Nb}_{1/2})\text{O}_3\text{-Pb}(\text{Mg}_{1/3}\text{Nb}_{2/3})\text{O}_3\text{-PbTiO}_3$ single crystals
J. Appl. Phys. **112**, 052006 (2012); 10.1063/1.4745979

Critical slowing down of relaxation dynamics near the Curie temperature in the relaxor $\text{Pb}(\text{Sc}_{0.5}\text{Nb}_{0.5})\text{O}_3$
Appl. Phys. Lett. **94**, 142906 (2009); 10.1063/1.3115765

Relaxation of induced polar state in relaxor $\text{PbMg}_{1/3}\text{Nb}_{2/3}\text{O}_3$ thin films studied by piezoresponse force microscopy
Appl. Phys. Lett. **86**, 222907 (2005); 10.1063/1.1942635

Domain structure and evolution in $(\text{PbMg}_{1/3}\text{Nb}_{2/3}\text{O}_3)_{0.75}(\text{PbTiO}_3)_{0.25}$ single crystal studied by temperature-dependent piezoresponse force microscopy
J. Appl. Phys. **97**, 094107 (2005); 10.1063/1.1890454

Direct piezoelectric effect in relaxor-ferroelectric single crystals
J. Appl. Phys. **95**, 5679 (2004); 10.1063/1.1703829



Launching in 2016!
The future of applied photonics research is here

OPEN ACCESS

AIP | APL Photonics

Multidimensional dynamic piezoresponse measurements: Unraveling local relaxation behavior in relaxor-ferroelectrics via big data

Rama K. Vasudevan,^{1,2} Shujun Zhang,³ M. Baris Okatan,^{1,2} Stephen Jesse,^{1,2} Sergei V. Kalinin,^{1,2} and Nazanin Bassiri-Gharb^{4,5,a)}

¹Center for Nanophase Materials Sciences, Oak Ridge National Laboratory, Oak Ridge, Tennessee 37831, USA

²Institute for Functional Imaging of Materials, Oak Ridge National Laboratory, Oak Ridge, Tennessee 37831, USA

³Department of Materials Science and Engineering, Materials Research Institute, Pennsylvania State University, University Park, Pennsylvania 16802, USA

⁴School of Materials Science and Engineering, Georgia Institute of Technology, Atlanta, Georgia 30332, USA

⁵G.W. Woodruff School of Mechanical Engineering, Georgia Institute of Technology, Atlanta, Georgia 30332, USA

(Received 28 October 2014; accepted 17 January 2015; published online 19 August 2015)

Compositional and charge disorder in ferroelectric relaxors lies at the heart of the unusual properties of these systems, such as aging and non-ergodicity, polarization rotations, and a host of temperature and field-driven phase transitions. However, much information about the field-dynamics of the polarization in the prototypical ferroelectric relaxor $(1-x)\text{Pb}(\text{Mg}_{1/3}\text{Nb}_{2/3})\text{O}_3$ - $x\text{PbTiO}_3$ (PMN- x PT) remains unprobed at the mesoscopic level. Here, we use a piezoresponse force microscopy-based dynamic multimodal relaxation spectroscopy technique, enabling the study of ferroelectric switching and polarization relaxation at mesoscopic length scales, and carry out measurements on a PMN-0.28PT sample with minimal polishing. Results indicate that beyond a threshold DC bias the average relaxation increases as the system attempts to relax to the previous state. Phenomenological fitting reveals the presence of mesoscale heterogeneity in relaxation amplitudes and clearly suggests the presence of two distinct amplitudes. Independent component analysis reveals the presence of a disorder component of the relaxation, which is found to be strongly anti-correlated with the maximum piezoresponse at that location, suggesting smaller disorder effects where the polarization reversal is large and vice versa. The disorder in the relaxation amplitudes is postulated to arise from rhombohedral and field-induced tetragonal phase in the crystal, with each phase associated with its own relaxation amplitude. These studies highlight the crucial importance of the mixture of ferroelectric phases in the compositions in proximity of the morphotropic phase boundary in governing the local response and further highlight the ability of PFM voltage and time spectroscopies, in conjunction with big-data multivariate analyses, to locally map disorder and correlate it with parameters governing the dynamic behavior. © 2015 AIP Publishing LLC. [<http://dx.doi.org/10.1063/1.4927803>]

I. INTRODUCTION

Nanoscale disorder in many systems gives rise to a number of unique emergent behaviors in materials ranging from martensites¹ and dipolar and spin glasses² to nematic liquid crystals³ and mixed valence manganese oxides.⁴ For instance, in perovskite systems with ferroic order parameters, the chemical disorder can lead to complete suppression of long-range ferroelectric order due to quenched random fields, as manifested in the “relaxor” crystals such as $\text{Pb}(\text{Mg}_{1/3}\text{Nb}_{2/3})\text{O}_3$ (PMN) or $\text{Pb}(\text{Zn}_{1/3}\text{Nb}_{2/3})\text{O}_3$ (PZN).⁵ Moreover, this disorder leads to a range of interesting and relatively poorly understood dynamic response characteristics, including broad dispersion of the dielectric response with a maximum shifting in temperature with measurement frequency,⁶ a variety of field- and temperature-induced phases,⁷ the existence of chemical nano-regions⁸ due to quenched phase fluctuations from the high temperature paraelectric state, and a critical slowing down of

dynamics⁹ below a characteristic freezing temperature, corresponding to a material transition to a non-ergodic state.¹⁰

Macroscopic electrical measurements of relaxors have revealed a wealth of intriguing phenomena in these systems, such as memory effects¹¹ and the wide distribution of relaxation times that give rise to non-exponential relaxations, and modelled by, e.g., the Kohlrausch-William-Watts (KWW) model.¹² But as compositional disorder lies at the heart of the unusual behavior of relaxors, knowledge at the atomic scale about ordering has been sought, with techniques such as diffuse scattering¹³ and pulsed neutron atomic pair-distribution function¹⁴ analysis used to study the short-range order and local environments of the ions.¹⁵ These studies have shown, e.g., the displacement of Pb^{2+} ions in the Pb-site along the $\langle 111 \rangle$ directions in PMN,¹⁶ and confirmed the existence of polar nanoregions (PNRs).^{17,18} Similarly, over the last decade, the mesoscopic heterogeneities that characterize relaxor systems have been accessible by local scanning probes since the advent of piezoresponse force microscopy (PFM), and a variety of PFM experiments have

^{a)}E-mail: nazanin.bassirigharb@me.gatech.edu

since revealed a wealth of information pertaining to frozen polarization at the surface as a result of mesoscopic symmetry breaking,¹⁹ differences in transition temperatures between bulk and surface,²⁰ spatial heterogeneity in local relaxation behaviors,²¹ and complex relaxation dynamics postulated to arise from fast and slow-responding polar nanoregions.²² Further, elemental mapping has been used to correlate chemical heterogeneity with local relaxation characteristics from PFM experiments.²³ The clear advantage of the local probe-based techniques is the ability to spatially map polarization behaviors and possibly correlate the heterogeneity in response with microstructural features or the chemical composition.

By chemical doping of PMN with a suitable amount of the prototypical ferroelectric PbTiO_3 , i.e., $(1-x)\text{Pb}(\text{Mg}_{1/3}\text{Nb}_{2/3})\text{O}_3-x\text{PbTiO}_3$ (PMN- x PT), it is possible to induce a ferroelectric phase that displays large electromechanical response, i.e., very high piezoelectric response in addition to very large electrostriction coefficients. These properties peak on the rhombohedral side of the morphotropic phase boundary (rhombohedral to monoclinic phase boundary at $x=0.305$ and monoclinic to tetragonal phase boundary at $x=0.355$ ²⁴ and their large electromechanical coupling has allowed these materials to be used in applications ranging from medical ultrasound devices to underwater sonar transducers,²⁵ sensors and actuators,²⁶ and micropositioners, and energy harvesting devices.^{27,28} However, there is a dearth of studies on these systems at the mesoscopic level by PFM beyond simple imaging of domain structures, and in particular, the relaxation behavior as a result of possible phase transitions,^{29,30} chemical heterogeneity, and their interaction with PNRs, in compositions in the vicinity of the MPB are unknown. Furthermore, much of the studies that do exist are of well-polished surfaces, to be more amenable for the atomic force microscope, although these polishing steps may alter the surface properties.³¹

Here, we present a PFM time and voltage-based (multimodal) spectroscopic measurement on the surface of an unpolished PMN-0.28PT sample and map properties spatially on mesoscopic scale. The results indicate that, on average, the system does not respond to small DC bias values, but beyond a threshold value, strong relaxation is observed and that relaxation is larger for higher bias pulses. Fitting of the relaxation curves provides evidence of two characteristic relaxation amplitudes, suggested to relate to rhombohedral and field-induced tetragonal phases, while multivariate statistical analysis reveals that the disorder in the relaxation amplitudes is highest when the field-induced polarization is small. Simulated datasets suggest that the disorder in the relaxation amplitudes is critical in explaining the heterogeneous nature of the relaxation across the surface. These studies suggest that the mixed-phase state in the ferroelectric relaxors is important in explaining the dynamic polarization response of ferroelectric relaxors near the MPB.

II. METHODS

A $\langle 001 \rangle$ cut single crystal sample of PMN-0.28PT was prepared by modified Bridgeman method and cut into

appropriate dimensions (thickness: $\sim 500 \mu\text{m}$) using a diamond saw. This composition is nominally rhombohedral, but is close enough to the MPB that we expect a phase mixture of rhombohedral and tetragonal phases (domains) to co-exist, or that alternatively, a tetragonal phase can be induced under application of a large enough DC bias. The sample was glued onto a sample plate with silver epoxy, which acted as the counter electrode and was grounded for the PFM measurements. The PFM experiments were performed in ambient conditions ($T \sim 20^\circ\text{C}$, $\text{RH} \sim 45\%$) with moderately stiff *Budget Sensors* cantilevers ($k \sim 1 \text{ N/m}$) and a free resonance (in air) of $\sim 75 \text{ kHz}$, on a *Cypher ES* AFM system from *Asylum Research*. *National Instruments* PXi-based cards were employed for signal generation and acquisition for the band-excitation (BE) experiments, which were performed using in-house scripts written in Labview v11 and Matlab v2011. All analyses were carried out using Matlab v2011.

The PFM spectroscopy experiment involves moving the tip across a pre-defined coordinate (x,y) grid on the sample and perturbing it with a DC bias waveform, and then measuring the response as a function of frequency via BE.^{21,32} BE involves generating a band of frequencies around the contact resonance and measuring the response over time, and subsequent Fourier transformation back to the frequency domain. This measurement is repeated for many time steps after each DC bias pulse; thus, at each (x,y) position, local spectroscopic information is acquired as a function of perturbation voltage (V) and time (t), and excitation frequency f , characterizing the system response $R = R(x,y,V,t,f)$. The response R at each (x,y,V,t) step is fit to a simple harmonic oscillator (SHO) function yielding the amplitude (A), phase (φ), quality factor (Q), and resonant frequency (ω) associated with the response. Throughout this manuscript, for the relaxation experiment, only the amplitude of the response at resonance is considered; thus, the final dataset is four dimensional, i.e., $A = (x,y,V,t)$ providing a 4D picture of voltage, time, and position-dependent polarization dynamics. We note here that given the PFM-based approach and the large sample thickness, one may assume that the conclusions derived are unique to the surface of the ferroelectric relaxor. However, the probed volume at the tip extends several ~ 10 s of nm into the crystal. Therefore, while we expect the conclusions derived from this experiment to be significantly affected by surface-related processes, the results are not completely dominated by the surface, i.e., we posit that we are measuring an interplay of surface and bulk-related relaxation processes.

III. BAND-EXCITATION EXPERIMENTAL RESULTS

A. Band-excitation piezoresponse force microscopy

A $2 \mu\text{m} \times 2 \mu\text{m}$ area of the sample was selected for the PFM spectroscopy experiment, and the topography of this area is plotted in Fig. 1(a). The topography appears extremely rough, as expected from an unpolished surface. Therefore, unlike previous experiments where polishing was carried out extensively to reduce surface roughness, here we work on unpolished samples that allow us to exclude the effects of any artefacts from these polishing steps. Note

however that the samples must be cut, though, and these have been diced using a diamond blade. The large roughness results in large shifts in the resonant frequency due to topographic variations and thus requires frequency tracking methods in PFM measurements. Therefore, to determine the domains structure, BE-PFM³³ experiments were performed in the same region, and the results (after SHO fitting) are plotted in Figs. 1(b)–1(d) with the BE-PFM amplitude, phase, and resonant frequency shown in Figs. 1(b), 1(c), and 1(d), respectively. The BE-PFM maps not only clearly show the presence of ferroelectric domains in the sample (evidenced by the change in phase), consistent with this composition of PMN-PT, but also indicate that there is considerable variation in the response within the large macrodomains, which suggests mesoscale heterogeneities affecting the amplitude of the piezoelectric response. It is important to note that the present instrumental resolution (~ 20 nm) precludes the ability to confirm or less the presence of nanodomains or clearly distinguish the presence of R and T phases, if intermixed at similar or smaller length-scales. The resonant frequency map in Fig. 1(d) indicates a very large variation in the stiffness of the tip-surface contact, as a result of the large roughness of the sample. Indeed, the shifts, according to this map, can be on the order of ~ 30 – 35 kHz and highlight the different elastic constraints (clamping) across the sample.

B. Dynamic multimodal spectroscopy

Having explored the domain structure, we now turn to obtaining dynamic spectroscopic information in the same

region. The $2\ \mu\text{m} \times 2\ \mu\text{m}$ area was divided into a 50×50 pixel grid (pitch: 40 nm), and the bias waveform plotted in Fig. 1(e) was applied to the tip at each grid-point. The waveform consists of a series of DC pulses of alternating polarity, with increasing amplitude up to ± 15 V. In between the DC pulses, the piezoresponse of the material is measured through application of a sequence of 8 BE-wave packets to the tip. A close-up view of the bias, measurement scheme, and waveforms is shown in Fig. 1(e) and its inset, where each orange dot indicates a point in time when the piezoresponse is measured. Note that only off-field (DC voltage = 0) segments of the response are discussed in this manuscript, although the in-field measurements were also recorded. After SHO fitting, the amplitude of the piezoresponse A is only the value at resonance frequency, and therefore a function of (x, y, V, t) .

The average amplitude response, A , across all (x, y) points is plotted in Fig. 2(a). The average sample response is plotted as a function of time, and the colors of the individual points reflect the time elapsed after the DC pulse immediately precedent to the measurement.³⁴ This graph clearly indicates the presence of two distinct regimes: for small voltages, there is minimal change in the system response, and little relaxation is evident. Beyond a threshold value, the material's response is clearly affected by the applied DC bias, and the degree of relaxation becomes progressively larger, i.e., the system attempts to revert to the initial state. The response at an individual point, for positive bias values, is shown in the waterfall-type plot in Fig. 2(b). Once again, the response appears to follow the same behavior where small bias does not perturb the system, and larger bias values

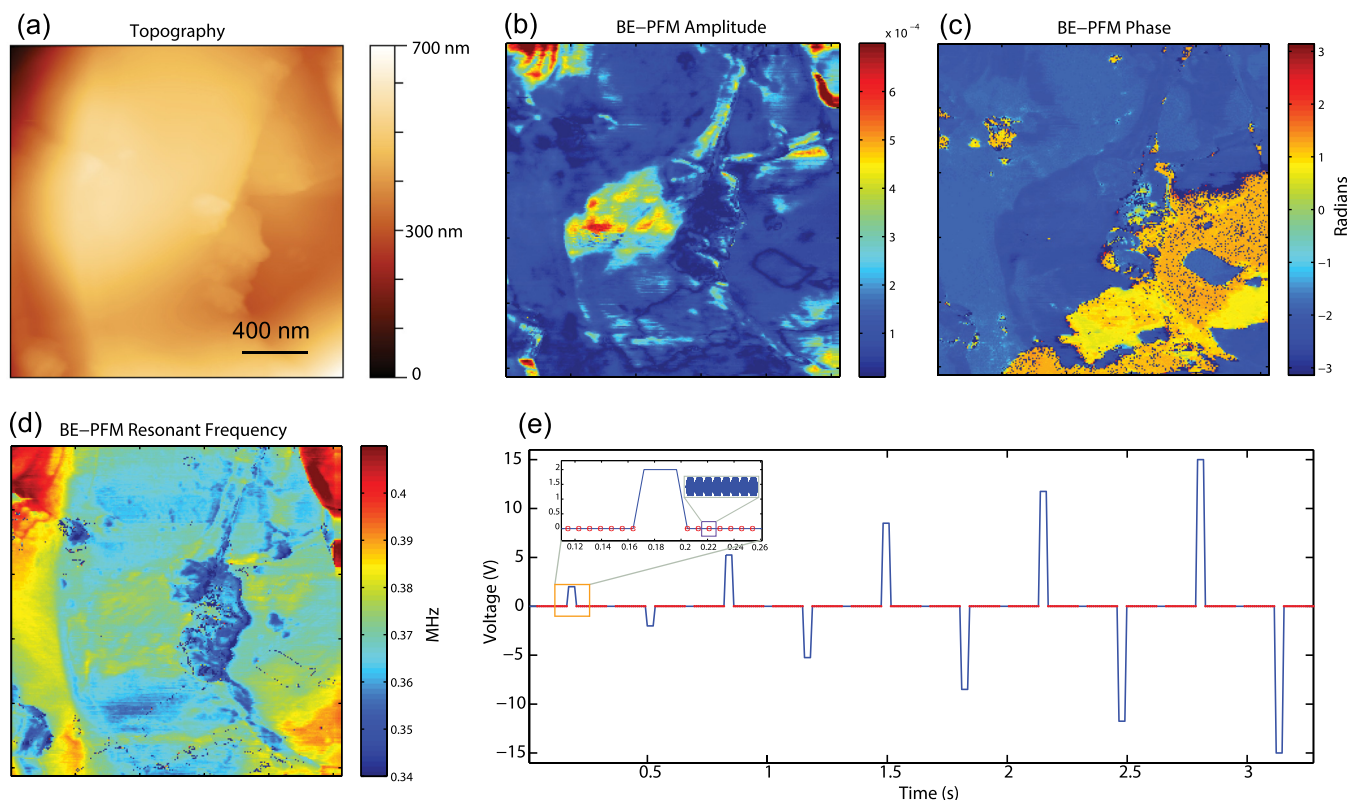


FIG. 1. Topography and band excitation piezoresponse force microscopy of PMN-0.28PT. (a) Topography, (b) vertical BE-PFM amplitude, (c) phase and (d) resonance maps. (e) DC waveform applied to the tip for multimodal measurement. The points where the piezoresponse is measured are indicated by the orange dots. All measurements were performed by BE-wave packets (shown inset).

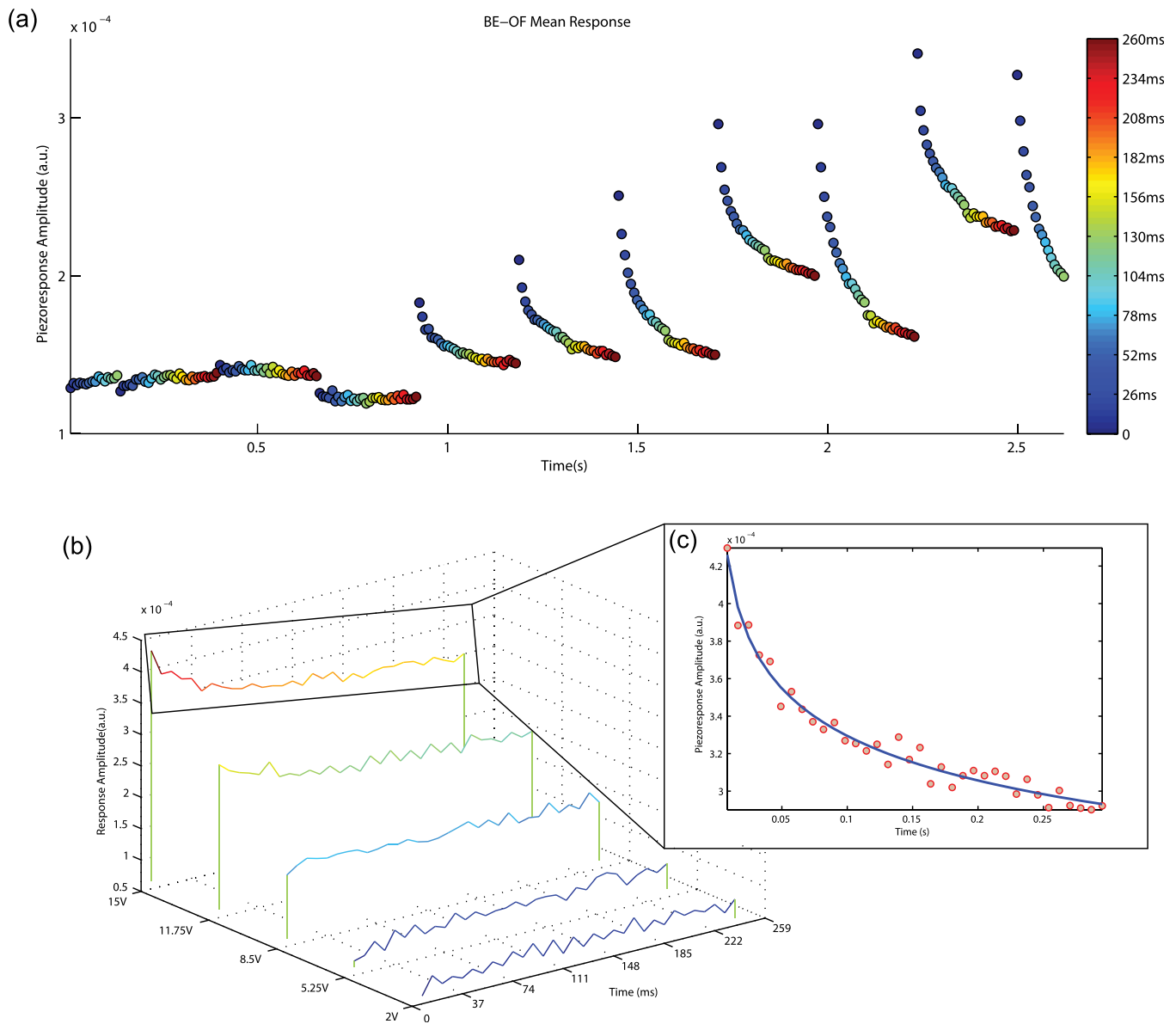


FIG. 2. Relaxation response on PMN-0.28PT. (a) Sample-averaged (all 2500 points) off-field piezoresponse amplitude for the (b) off-field response at an individual point, as a function of voltage (only positive bias responses are shown here, for clarity). (c) Sample fitting of response vs. time to a stretched exponential function, at a single voltage step ($V = 15$ V).

result in significant perturbation of the system and subsequent relaxation.

C. Functional fitting approaches

In order to gain an understanding of the relaxation data, we first employ the KWW exponential fitting model

$$A(x, y, V, t) = A_0(x, y, V) + R_0(x, y, V) \exp \left[- \left(\frac{t}{\tau_{KWW}(x, y, V)} \right)^\beta \right], \quad (1)$$

with $0 < \beta \leq 1$. As an example, the fit for a single point at $V = 15$ V is shown in Fig. 2(c). These fittings result in spatial maps for A_0 , the relaxation amplitude R_0 , relaxation time τ , and the KWW exponent β as a function of the DC pulse

voltage. The maps for the relaxation amplitude R_0 for the two largest positive and negative voltages are shown in Figs. 3(a) and 3(b) and Figs. 3(d) and 3(e), respectively (full maps shown in Supplementary Material³⁵ S1 and S2). These maps show considerable variation in the relaxing amplitude, which indicates the presence of mesoscopic disorder, and appear to show some degree of clustering of the high and lower response regions. Note that points where the stretched exponential fit was poor are excluded from the spatial maps (hence resulting in white pixels) and all the subsequent histograms. Direct correlation with the PFM maps in Fig. 1 is also limited. The histograms for R_0 , at $V = \pm 15$ V (plotted in Figs. 3(c) and 3(f)), show distributions that are well fit by two Gaussians (note that the behavior of R_0 for the other voltages above threshold value is similar). The two distributions of the relaxation amplitude may be related to the presence of rhombohedral and field-induced tetragonal phases, which

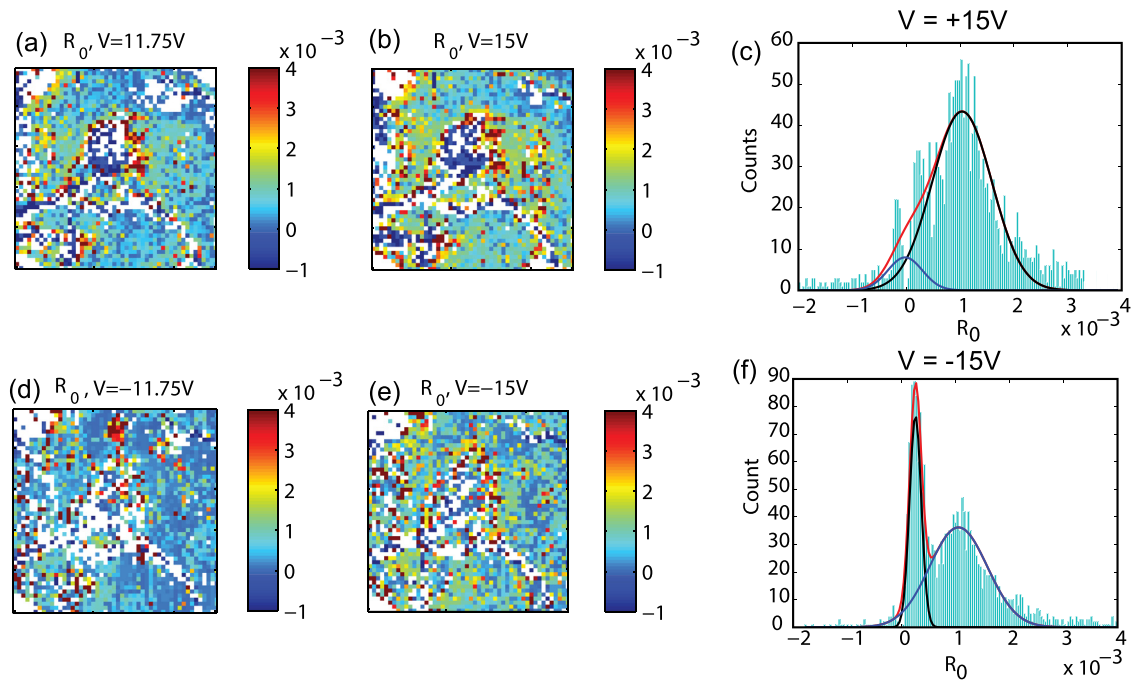


FIG. 3. Spatial maps of R_0 . Maps for positive bias values are shown in (a) and (b) and maps for negative bias values are shown in (d) and (e). (c) and (f) Histograms with double Gaussian fit for R_0 ($V = 15$ V) and R_0 ($V = -15$ V), respectively. Note that white pixels are locations where the fitting was poor and thus neglected; these points are also excluded from the associated histograms.

can be expected to have different characteristic relaxation amplitudes due to differing levels of degeneracy and is discussed later. Note that for simplicity, here we refer only to the field-induced tetragonal phase. However, all discussions are consistent with the presence of alternative or coexistent (field-induced) monoclinic phase.

Interestingly, the maps for the relaxation time τ , shown in Figs. 4(a) and 4(b) do not show as much heterogeneity for the positive bias values. Slightly more heterogeneity is seen for

the negative bias, plotted in Figs. 4(d) and 4(e), but the relaxation times for both biases are still extremely small as evidenced by the histograms in Figs. 4(c) and 4(f) for $V = \pm 15$ V (Supplementary Material S1 and S2 for full maps). In other words, the reason for the non-Gaussian distribution of τ is that relaxation occurs on a timescale faster than the temporal resolution of the experiment. Note that the points that are red in the spatial maps are points where there is little relaxation. These points are fairly well correlated for different voltages of

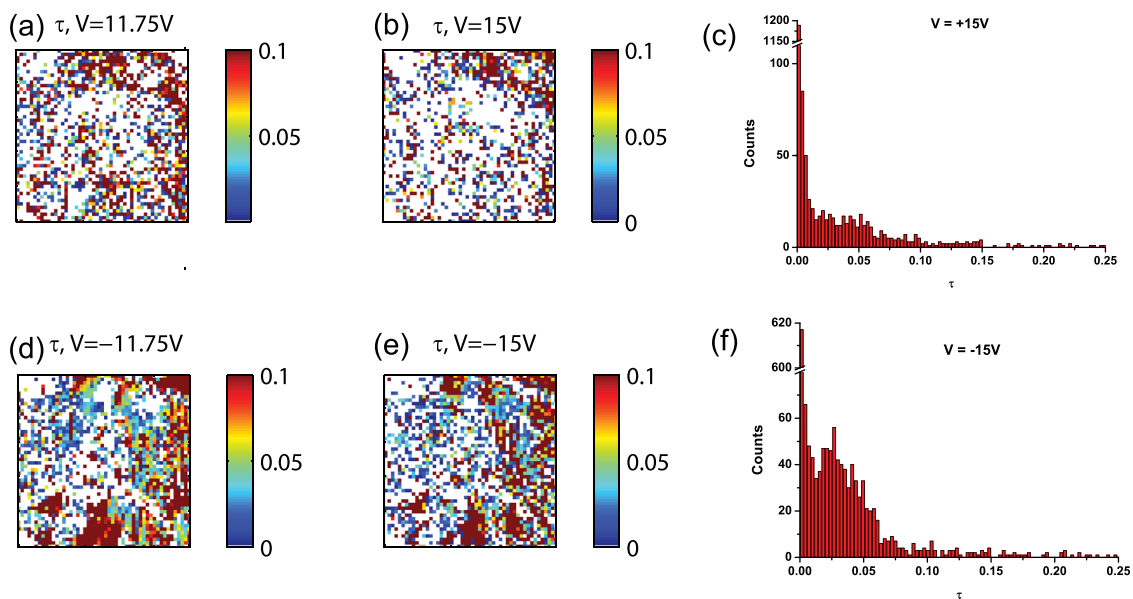


FIG. 4. Spatial maps of τ . Maps for the two highest positive bias values ($V = 11.75$ V and $V = 15$ V) are shown in (a) and (b). (c) Histogram τ ($V = +15$ V). The maps for the two most negative bias values are shown in (d) and (e), and the histogram for τ ($V = -15$ V) is shown in (f). Only τ values less than 0.25 are shown in the histograms. Note that white pixels are locations where the fitting was poor and thus neglected; these points are also excluded from the associated histograms. Additionally, some white pixels in the spatial maps are of locations where the value of τ is extremely small (<0.001).

the same *polarity*, i.e., the red points in Fig. 4(d) correlate well with the red pixels in Fig. 4(e), but do not necessarily correlate with the points with low relaxation in opposite polarity. This difference may be related to the stability of the polarization orientation. Therefore, the red points in these maps may correspond to areas where the stability of the ferroelectric phase is high, and the difference between the polarities is indicative of built-in fields asymmetrizing the potential well and favoring specific orientation(s) over others.

We now turn our attention to the KWW exponent β , the maps of which are plotted for $V = +15$ V and $V = -15$ V in Figs. 5(a) and 5(c) (full maps provided in Supplementary Material S3 and S4). The corresponding histograms are shown next to the spatial maps in Figs. 5(b) and 5(d) and reveal that a limited number of points, ~ 90 points for positive bias and ~ 300 points for negative bias, show a stretch exponent of 1, and therefore are due to Debye-type relaxation. Although there is significant dispersion, there appears to be some clustering around $\beta \sim 0.12$ and $\beta \sim 0.15$ for positive and negative, respectively. These values are lower than those measured for PMN-10PT,²² where $\beta \sim 0.3$ was found. For stretched exponential relation, the stretch exponent β is essentially a measure of the steepness of the relaxation behavior, with smaller values corresponding to slower (more shallow) relaxation and larger values corresponding to faster (i.e., steeper) relaxation curve.

D. Independent component analysis

The functional fitting shows intriguing heterogeneities in the responses of the different fitting parameters, yet the precise nature of the disorder in the crystal is obscure, due to the imposition of phenomenological fitting functions on the

relaxation response. In order to circumvent this problem, we turn to multivariate statistical analysis, specifically independent component analysis (ICA³⁶), to re-analyze the data. In ICA, we begin with a given set of observation of random variables (in this case, the relaxation response) $(R_1(t), R_2(t), \dots, R_n(t))$, where t is time, and we postulate that the signal is generated as a linear mixture of independent components s_i (here, limited to two³⁷), i.e.,

$$\begin{pmatrix} R_1(t) \\ \dots \\ R_n(t) \end{pmatrix} = \mathbf{A} \begin{pmatrix} s_1(t) \\ s_2(t) \end{pmatrix}, \quad (2)$$

where \mathbf{A} is some unknown mixing matrix. The task of ICA is to then estimate both matrix \mathbf{A} and $s_i(t)$. Broadly, independence requires that the components be maximally non-Gaussian. If we assume that the dynamic behavior of the ferroelectric relaxor is governed by two relaxation processes that are independent of each other and independent of voltage, then we may write the amplitude of the piezoresponse at each position $A = A(x, y, V, t)$ as

$$A(x, y, V, t) = c_1(x, y, V)s_1(t) + c_2(x, y, V)s_2(t), \quad (3)$$

and ICA can be used to determine the independent components $s_1(t)$ and $s_2(t)$ and the mixing coefficients c_1 and c_2 .³⁸ The results of the ICA analysis (after 50 iterations, to confirm repeatability of the analysis) are shown in Fig. 6, with spatial maps of c_1 and c_2 plotted for $V = 8.5, 11.75,$ and 15 V alongside the components. While only the positive segments of the waveform are reported, the negative segments show similar behavior (Supplementary Material S5). It is noteworthy to remember that in ICA, components may arbitrarily flip

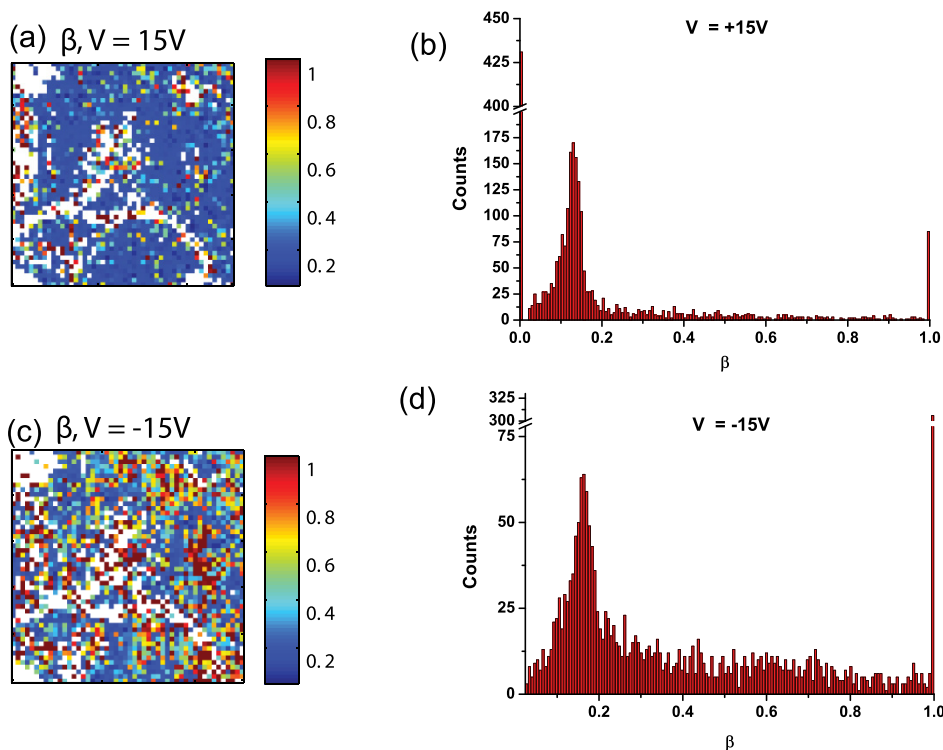


FIG. 5. Spatial maps of KWW exponent. The spatial maps for β are shown for (a) $+15$ V and (c) -15 V. The histograms of β corresponding to these voltages are shown below the respective spatial maps for (b) $V = +15$ V and (d) $V = -15$ V. Note that white pixels are locations where the fitting was poor and thus neglected; these points are also excluded from the associated histograms.

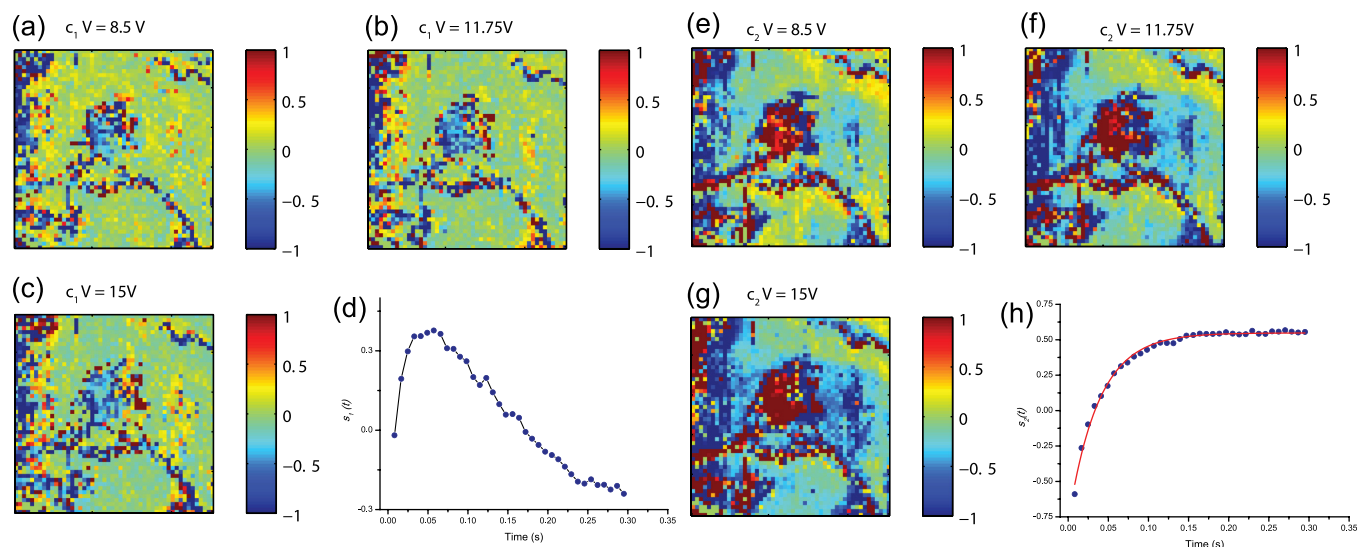


FIG. 6. Independent component analysis of the positive segments. (a)–(c) Maps of mixing coefficients c_1 are shown for three different voltages. (d) $s_1(t)$ is plotted. Similarly, maps of c_2 are shown for three different voltages in (e)–(g), with $s_2(t)$ plotted in (h). There is a little variation in the spatial maps for $s_1(t)$ with respect to voltage, suggesting that the disorder term ($s_1(t)$) reflects the quenched disorder.

sign and further are ordered arbitrarily (unlike in principal component analysis³⁹), but in the case of sign flipping, the mixing coefficients can compensate accordingly. The component $s_2(t)$, plotted in Fig. 6(h), shows a curve that is well fit by a standard exponential function, which is plotted as a red line. However, the other component $s_1(t)$, shown in Fig. 6(d), shows a pronounced increase in the initial stages followed by a decrease. Essentially, the mixing of these two components will result in a relaxation response that is somewhat slower, strongly suggesting that this component is correlated with the disorder in the material. Therefore, maps of the mixing coefficient c_1 should produce a map of the surface highly correlated to the degree of local disorder. Indeed, the maps of c_1 in Figs. 6(a)–6(c) show that small, ~ 200 nm sized regions display large values, indicative of mesoscopic disorder. There is also minimal variation across voltage slices, suggesting that we are indeed measuring the quenched disorder.

To attempt to correlate the disorder with the piezoresponse, we report also the piezoresponse as measured immediately after the bias pulse for the two largest positive bias values, in Figs. 7(a) and 7(b) (full maps for positive and negative bias in Supplementary Material S6 and S7). These maps show considerable variation, as expected, but the remarkable aspect is that the regions which show high

response in Fig. 7 appear to display significantly lower disorder (Figs. 6(a)–6(c)). That is, the high piezoresponse at these points coincides with decreasing influence of disorder on the relaxation response, suggesting that the disorder is weak in the regions with the strongest ferroelectric nature of the sample, which (presumably) correspond to areas where NPR fraction is small. This is further confirmed by scatter plots of the piezoresponse amplitude immediately after the bias pulse and the mixing coefficient c_1 from the ICA (supplementary S8). Therefore, the independent component analysis is clearly much more adept at discovering the regions of disorder than the traditional functional fitting approach, which often fails due to the signal-to-noise ratio at each point, i.e., noise in the signal results in uncertainties that are higher than the uncertainties in the model. With ICA, however, the entire dataset is considered and there are no constraints imposed by the model, so long as the components themselves are maximally independent.

E. Source of disorder

It is still unclear whether the disorder is induced by the presence of different relaxation times or is instead the result of two different events with different relaxation amplitudes, since the temporal resolution of the experiment did not allow

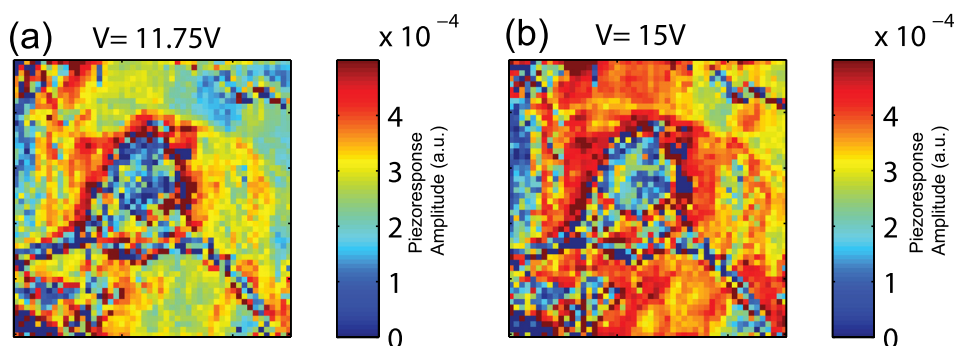


FIG. 7. Piezoresponse at the first time step. Piezoresponse maps measured immediately after bias application for $V =$ (a) 11.75 V and (b) 15 V.

determination of the distribution of τ for very fast relaxations. As a result, we turn to simulated datasets on which we perform the same ICA analysis. Datasets were formed with the general form of the relaxation response estimated as

$$R(x, y, t) = A_0(x, y) + R_0(x, y)\exp\left(-\frac{t}{\tau_1(x, y)}\right) + R_1(x, y)\exp\left(-\frac{t}{\tau_2(x, y)}\right), \quad (4)$$

with normally distributed values for parameters A_0 , R_0 , R_1 , τ_1 , and τ_2 . Note that all of these parameters were simulated to be position dependent. The mean values used for the parameters were similar to those we observe in experiments. We first turn to the limiting case when the relaxation times τ are the same, i.e., $\tau_1 = \tau_2$ and observe the results of the signal de-mixing. The ICA was carried out for the simulated dataset, again assuming that the response is a mixture of two distinct signals, and the results are plotted in Figs. 8(a) and 8(b). The distribution of the parameters is shown in the histograms in Figs. 8(c)–8(e). Interestingly, the independent components look very similar to $s_1(t)$ and $s_2(t)$ calculated for the real data in Fig. 6. We also considered the other limiting case when the relaxation amplitudes R_0 and R_1 are equal, i.e.,

$$R(t) = A_0(x, y) + R_0(x, y)\exp\left(-\frac{t}{\tau_1(x, y)}\right) + R_0(x, y)\exp\left(-\frac{t}{\tau_2(x, y)}\right), \quad (5)$$

i.e., with the disorder in the relaxation times, but not in the amplitude. The resulting components from ICA of this dataset are only exponential and do not show the features that are evident in $s_1(t)$ (Supplementary Material S9). Therefore, we conclude that disorder in the relaxation amplitude is sufficient to reproduce qualitatively the signals observe in the real dataset. While it is possible that there exists disorder in both terms (Supplementary Material S10), this cannot be verified by the measurement.

We conclude that in the experimental data, the reason for the observed disorder component can be ascribed to the existence of two processes with distinct relaxation amplitudes and independent spatial distribution. Any eventual variations in the relaxation time constants cannot be captured at this time within instrumental resolution. This is unlikely, however, due to physical reasons, since the PNRs which can be present in the material are likely to relax at much slower time scales¹⁹ at this temperature. Next, we consider a different mechanism to explain the results, involving the mixture of R and T-phases that can be present in these systems.

F. Extended discussion

In order to explain the experimental and modeling observations, we consider that since the material is nominally close to the morphotropic phase boundary, and so the rhombohedral phase, due to the presence of local defects, chemical heterogeneity and/or elastic boundary conditions are susceptible to a field-induced transition to a tetragonal phase. The degree of susceptibility to such phase transition is expected to vary across the sample surface on the mesoscale,

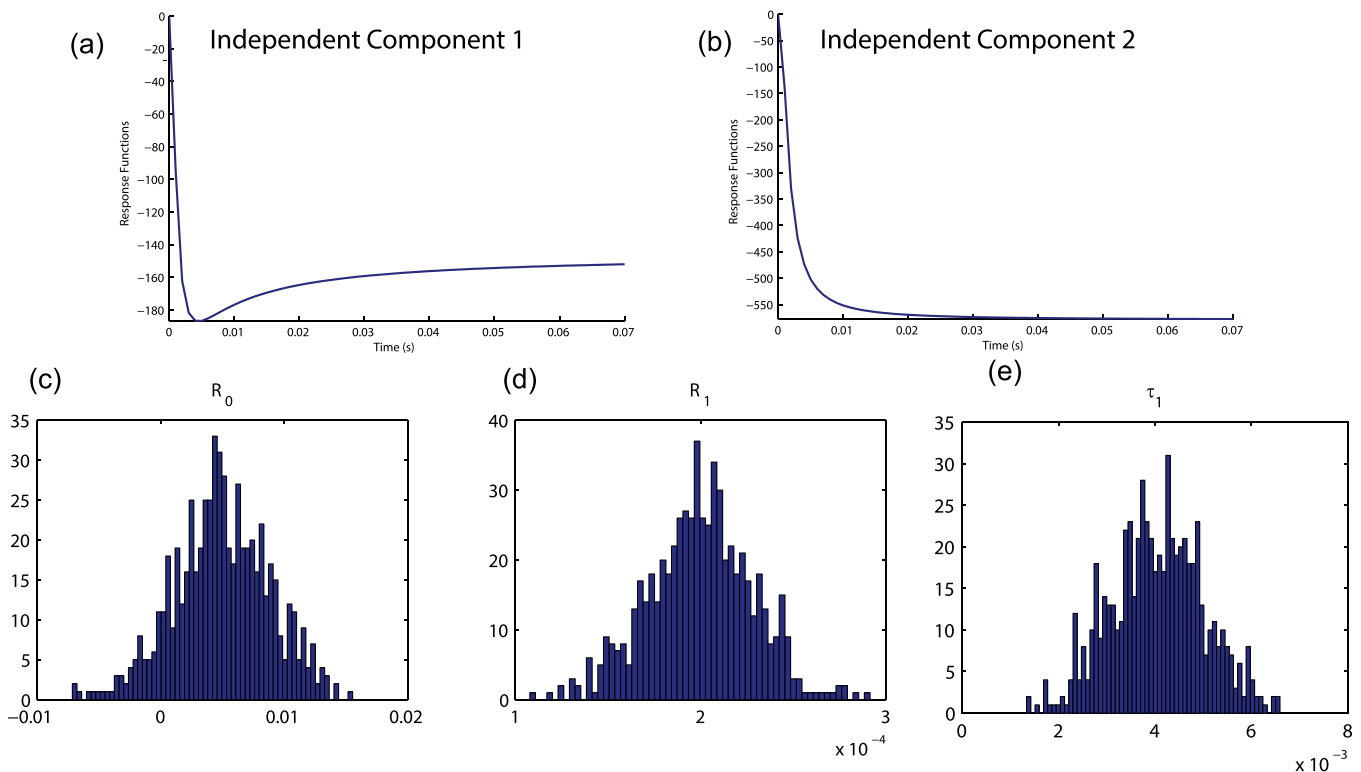


FIG. 8. Simulated dataset for ICA. The ICA is performed on a *simulated* dataset with disorder in the relaxation amplitude, but not in the relaxation times. (a) and (b) ICA components from analysis based on (c) and (d) distributions of R_0 and R_1 and (e) distributions of τ_1 . Such datasets can indeed result in components similar to the experimentally observed components (Fig. 6). The effect of the disorder component is to delay the relaxation of the response slightly.

as a result of the above three factors. For low bias values, there is little response because the rhombohedral phase in the (001)-oriented crystal has ferroelastically degenerate out of plane components of polarization, which suggests that the maximum response is only obtained during 180° (ferroelectric) switching. When the applied bias is increased, the areas where the threshold field for the R → T transition is exceeded will result in much larger response due to the field-induced polarization rotation. At the same time, as the material is a single crystal with more stringent boundary conditions than, e.g., polycrystalline films, the newly formed domains are expected to be unstable in the absence of the field and is subject to substantial relaxation, which is what is observed. The degree of relaxation of the response is a function of the stability of the newly formed domains, which in turn is dictated by the local elastic^{40,41} and electric boundary conditions (compatibility of variants^{42,43}), local defects, etc. Therefore, two characteristic relaxing *amplitudes*, corresponding to the rhombohedral phase and (field-induced) tetragonal phase, based on the differing number of degenerate states and strains correlated to the relaxation process, are expected and indeed this is also observed. We cannot detect the presence of two characteristic relaxation times, but we note that they may exist below the time scale of the temporal resolution of the instrument. The effect of the disorder is lower in areas of large piezoelectric response, i.e., relaxation is fast, due to the higher degree of R → T phase transition at these sites, whereas those areas where there is a smaller degree of relaxation are more prone to longer relaxation times, due to the higher degree of stability of the switched R-phase.

Finally, we note the role of the PNRs appears minimal in these experiments, due to the fact that the majority of the material is expected to be in the ferroelectric phase and indeed appears to behave in this manner (short relaxation times, large piezoelectric response, and characteristic domains). However, due to chemical disorder inherent to the relaxor-ferroelectric solutions, there is still likely to be a different fraction of ferroelectric R phase and PNRs in the volume probed by the tip at each spatial location. Then, the different fractions of R phase and PNRs, the degree of susceptibility of R→T transition, and the degree of field-induced transition from PNR → ferroelectric phase are all responsible for the relaxation response. But we posit that these are likely only weakly affecting the relaxation behavior in our sample, as significant influence of PNRs is expected to result in very long relaxation times, which are not observed.¹⁹

IV. SUMMARY AND CONCLUSIONS

A multidimensional technique was implemented utilizing band-excitation piezoresponse force microscopy to map the spatial disorder in the relaxor ferroelectric crystal PMN-0.28PT, which consists of a DC pulse train of increasing amplitude and dual-polarity, with measurement of the piezoresponse signal after each pulse. The measurements reveal clear mesoscopic heterogeneity in the relaxation response across the surface of the sample. Phenomenological fitting to the

relaxation response at each point with the stretched exponential function revealed the value of the exponent (β) was ~ 0.15 , while histograms for the relaxing amplitude indicated the presence of two distinct peaks. The calculation of the relaxation time τ showed very short relaxation times, indicative of fast relaxation processes. Given the significant size of the data that is produced by multidimensional scanning probe microscopy techniques, “big-data” style analysis consisting of multivariate statistical analysis was undertaken to understand the data, specifically through use of the independent component analysis method. The analysis revealed the presence of an exponential relaxation component and a second disorder component, which correlated with the low response regions of the film. Furthermore, simulated datasets reveal that the data can be reconstructed by considering only the disorder in the relaxing amplitudes. It is suggested that the cause of the mesoscopic heterogeneities in the PMN-0.28PT relaxor are the differing fractions of rhombohedral and field-induced tetragonal phase in the volume of material probed under the tip. These studies highlight the importance the mixture of R and field-induced T phases in the relaxor-ferroelectric in proximity of the morphotropic phase boundary in governing the local relaxation response.

ACKNOWLEDGMENTS

This research was sponsored by the Division of Materials Sciences and Engineering, BES, DOE (R.K.V. and S.V.K.). A portion of this research was conducted at and partially supported by (S.J. and M.B.O.) the Center for Nanophase Materials Sciences, which is a DOE Office of Science User Facility. N.B.-G. acknowledges funding from the U.S. National Science Foundation through Grant No. DMR-1255379.

¹R. J. D. Tilley, *Understanding Solids: The Science of Materials* (Wiley, 2013).

²H. Mönig, M. Todorovic, M. Z. Baykara, T. C. Schwendemann, L. Rodrigo, E. I. Altman, R. Pérez, and U. D. Schwarz, *ACS Nano* **7**, 10233 (2013).

³T. Araki, M. Buscaglia, T. Bellini, and H. Tanaka, *Nat. Mater.* **10**, 303 (2011).

⁴M. B. Salamon and M. Jaime, *Rev. Mod. Phys.* **73**, 583 (2001).

⁵A. Bokov and Z.-G. Ye, *Frontiers of Ferroelectricity* (Springer, 2007), p. 31.

⁶A. Levstik, Z. Kutnjak, C. Filipič, and R. Pirc, *Phys. Rev. B* **57**, 11204 (1998).

⁷B. Dkhil and J. M. Kiat, *J. Appl. Phys.* **90**, 4676 (2001).

⁸F. Jiang, S. Kojima, C. Zhao, and C. Feng, *Appl. Phys. Lett.* **79**, 3938 (2001).

⁹D. Viehland, S. J. Jang, L. E. Cross, and M. Wuttig, *J. Appl. Phys.* **68**, 2916 (1990).

¹⁰Z. Kutnjak, C. Filipič, R. Pirc, A. Levstik, R. Farhi, and M. El Marssi, *Phys. Rev. B* **59**, 294 (1999).

¹¹G. Xu, P. Gehring, and G. Shirane, *Phys. Rev. B* **72**, 214106 (2005).

¹²K. Binder and W. Kob, *Glassy Materials and Disordered Solids: An Introduction to Their Statistical Mechanics* (World Scientific, 2011).

¹³D. J. Goossens, *Acc. Chem. Res.* **46**, 2597 (2013).

¹⁴T. Egami, *Local Structure from Diffraction* (Springer, 2002), p. 1.

¹⁵B. Dkhil, J. Kiat, G. Calvarin, G. Baldinozzi, S. Vakhrushev, and E. Suard, *Phys. Rev. B* **65**, 024104 (2001).

¹⁶K. Fujishiro, T. Iwase, Y. Uesu, Y. Yamada, B. Dkhil, J.-M. Kiat, S. Mori, and N. Yamamoto, *J. Phys. Soc. Jpn.* **69**, 2331 (2000).

¹⁷M. E. Manley, J. W. Lynn, D. L. Abernathy, E. D. Specht, O. Delaire, A. R. Bishop, R. Sahul, and J. D. Budai, *Nat. Commun.* **5**, 3683 (2014).

- ¹⁸I.-K. Jeong, T. Darling, J. Lee, T. Proffen, R. Heffner, J. Park, K. Hong, W. Dmowski, and T. Egami, *Phys. Rev. Lett.* **94**, 147602 (2005).
- ¹⁹A. Kholkin, A. Morozovska, D. Kiselev, I. Bdikin, B. Rodriguez, P. Wu, A. Bokov, Z. G. Ye, B. Dkhil, L. Q. Chen, M. Kosec, and S. V. Kalinin, *Adv. Funct. Mater.* **21**, 1977 (2011).
- ²⁰V. Shvartsman, B. Dkhil, and A. Kholkin, *Annu. Rev. Mater. Res.* **43**, 423 (2013).
- ²¹S. V. Kalinin, B. J. Rodriguez, S. Jesse, A. N. Morozovska, A. A. Bokov, and Z.-G. Ye, *Appl. Phys. Lett.* **95**, 142902 (2009).
- ²²S. V. Kalinin, B. J. Rodriguez, J. D. Budai, S. Jesse, A. N. Morozovska, A. A. Bokov, and Z. G. Ye, *Phys. Rev. B* **81**, 064107 (2010).
- ²³Q. Li, Y. Liu, Z. Cheng, J. Bian, H. Chen, and R. L. Withers, *Appl. Phys. Lett.* **103**, 022904 (2013).
- ²⁴F. Li, S. Zhang, Z. Xu, X. Wei, J. Luo, and T. R. Shrout, *J. Appl. Phys.* **108**, 034106 (2010).
- ²⁵S. Zhang, F. Li, J. Luo, R. Sahul, and T. R. Shrout, *IEEE Trans. Ultrason. Ferroelectr.* **60**, 1572 (2013).
- ²⁶S. E. Park and T. R. Shrout, *Mater. Res. Innov.* **1**, 20 (1997).
- ²⁷K. Ren, Y. Liu, X. Geng, H. F. Hofmann, and Q. M. Zhang, *IEEE Trans. Ultrason. Ferroelectr.* **53**, 631 (2006).
- ²⁸S. Priya, *J. Electroceram.* **19**, 167 (2007).
- ²⁹P. Finkel, K. Benjamin, and A. Amin, *Appl. Phys. Lett.* **98**, 192902 (2011).
- ³⁰M. Shen, G. G. Siu, Z. K. Xu, and W. Cao, *Appl. Phys. Lett.* **86**, 192902 (2005).
- ³¹M. F. Wong and K. Zeng, *J. Am. Ceram. Soc.* **94**, 1079 (2011).
- ³²S. Jesse, S. V. Kalinin, R. Proksch, A. P. Baddorf, and B. J. Rodriguez, *Nanotechnology* **18**, 435503 (2007).
- ³³R. K. Vasudevan, S. Jesse, Y. Kim, A. Kumar, and S. V. Kalinin, *MRS Commun.* **2**, 61 (2012).
- ³⁴The time scale here is somewhat less than the entire waveform in Fig. 1(e), due to the neglected points from the in-field measurement. Additionally, “0 V” is considered a pulse, so there are 9 measurement sets.
- ³⁵See supplementary material at <http://dx.doi.org/10.1063/1.4927803> for supplementary information document.
- ³⁶A. Hyvärinen, J. Karhunen, and E. Oja, *Independent Component Analysis* (John Wiley & Sons, 2004), Vol. 46.
- ³⁷Larger systems were considered; however, the resulting independent signals suggested that only two independent systems might be present.
- ³⁸A voltage dependence for the components can also be preserved in the ICA decomposition, i.e., setting $s_i = s_i(V,t)$. However, such analysis produced very similar components to the voltage-independent case and thus we transform the problem into a simpler one in which the components are no longer varying with voltage.
- ³⁹S. Jesse and S. V. Kalinin, *Nanotechnology* **20**, 085714 (2009).
- ⁴⁰Y. Ivry, J. F. Scott, E. K. H. Salje, and C. Durkan, *Phys. Rev. B* **86**, 205428 (2012).
- ⁴¹Y. Ivry, C. Durkan, D. Chu, and J. F. Scott, *Adv. Funct. Mater.* **24**, 5567 (2014).
- ⁴²N. Tsou and J. Huber, *Mech. Mater.* **42**, 740 (2010).
- ⁴³N. T. Tsou and J. E. Huber, *Continuum Mech. Thermodyn.* **22**, 203 (2010).